JOURNAL OF GEOPHYSICAL RESEARCH, VOL. 107, NO. D20, 4448, doi:10.1029/2001JD000935, 2002

1DVAR analysis of temperature and humidity using GPS radio occultation refractivity data

Paul Poli[1]
Joint Center for Earth Systems Technology, University of Maryland Baltimore County, Baltimore, Maryland, USA

Joanna Joiner
Laboratory for Atmospheres, NASA Goddard Space Flight Center, Greenbelt, Maryland, USA

E. Robert Kursinski[2]
University of Arizona, Tucson, Arizona, USA

Received 12 June 2001; revised 30 April 2002; accepted 1 May 2002; published 30 October 2002.

[1] The constellation of Global Positioning System (GPS) satellites provides a source of continuous, phase-stable electromagnetic signals available for radio occultation observations of our planet. The atmospheric-induced bending of the transmitted rays observed during each occultation can be converted into a refractivity profile using an Abel transform. Since refractivity is related to temperature and humidity, it may potentially be used in global data assimilation for numerical weather prediction (NWP) and for creating climate data sets. We first compare GPS/Meteorology (GPS/MET) 1995 refractivity with various backgrounds and verify that the best expected background presents generally the best fit with the observed refractivity. We implement here an efficient one-dimensional variational (1DVAR) analysis of GPS refractivity that enables retrieving temperature, humidity, and sea-level pressure using the finite volume data assimilation system background. 1DVAR analyses with GPS/MET 1995 data are compared with collocated radiosondes. They show an excellent capacity of the GPS measurements to resolve the tropopause. In the Northern Hemisphere, we demonstrate a net reduction of temperature bias and standard deviation, as compared with the background. The 1DVAR humidity presents reduced standard deviation as compared to the background between 550 and 400 hPa. However, a refractivity bias between the observations and the background in the lower troposphere systematically shifts the 1DVAR humidity downward. A refractivity bias over the whole profile is transformed into a 1DVAR sea-level pressure bias. This study represents a step toward using the GPS radio occultation data in data assimilation systems to improve NWP forecasts and representation of Earth's climate in models. *INDEX TERMS:* 3337 Meteorology and Atmospheric Dynamics: Numerical modeling and data assimilation; 3360 Meteorology and Atmospheric Dynamics: Remote sensing; 3394 Meteorology and Atmospheric Dynamics: Instruments and techniques; 6904 Radio Science: Atmospheric propagation; *KEYWORDS:* GPS, radio occultation, refractivity, data assimilation, radiosonde, 1DVAR

Citation: Poli, P., J. Joiner, and E. R. Kursinski, 1DVAR analysis of temperature and humidity using GPS radio occultation refractivity data, *J. Geophys. Res.*, *107*(D20), 4448, doi:10.1029/2001JD000935, 2002.

1. Introduction

[2] The Global Positioning System (GPS) system provides continuous radio signals for precise positioning in the immediate vicinity of our planet. The atmosphere affects the speed of propagation of these signals. These perturbations in the GPS signals can in turn be used to remotely sense the atmosphere. In particular, by placing a receiver in Low Earth Orbit (LEO), for example, 500 to 2000 km altitude, it is possible to perform soundings using the limb-viewing radio occultation technique. Radio occultation has been used for more than 30 years to study the atmospheres of other planets [e.g., *Fjeldbo et al.*, 1971; *Lindal et al.*, 1979, 1981; *Tyler et al.*, 1982; *Lindal*, 1992; *Jenkins et al.*, 1994]. *Gorbunov and Sokolovskiy* [1993] provided simulations of GPS radio occultation measurements. *Kursinski et al.* [1997] also simulated many aspects of GPS measurements and their expected error characteristics. GPS/Meteorology (GPS/MET, 1995) was the first radio occultation experiment conducted on Earth using radio occultation [e.g., *Kursinski et al.*, 1996; *Ware et al.*, 1996; *Rocken et al.*, 1997].

[1] Also at Météo France, Centre National de Recherches Météorologiques (GMAP), Toulouse, France.
[2] Also at NASA Jet Propulsion Laboratory, California Institute of Technology, Pasadena, California.

0148-0227/02/2001JD000935$09.00

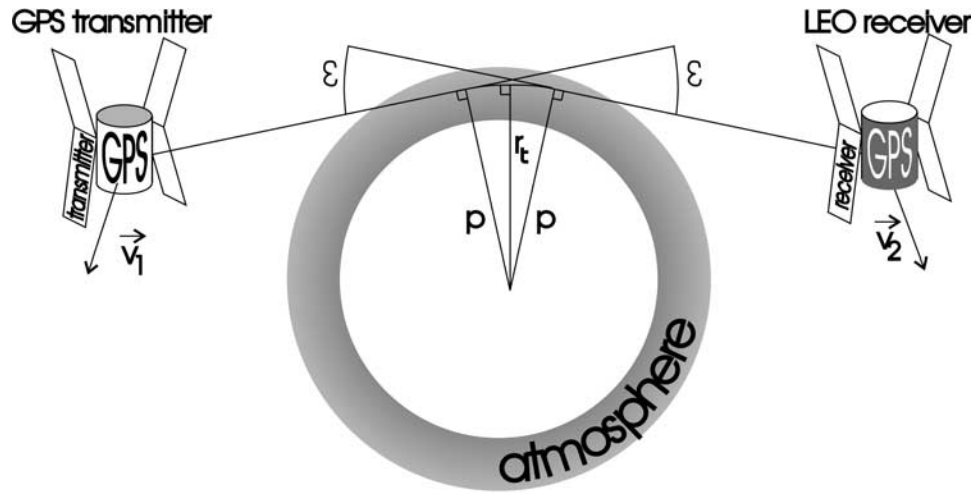

Figure 1. Geometry of a GPS occultation under the hypothesis of spherical symmetry of the atmosphere.

[3] In this work, we have developed a one dimensional variational (1DVAR) analysis of temperature, humidity and sea-level pressure. In this approach, background information is used to constrain the retrievals. The scheme implemented here uses GPS refractivity, whereas *Palmer et al.* [2000] used GPS bending angles. *Healy and Eyre* [2000] developed a 1DVAR with GPS refractivity that they used for a simulation study. *Kursinski et al.* [2000a] also developed a 1DVAR and used it with GPS/MET refractivity observations and a ECMWF background. They discussed the latitude versus height differences created by the 1DVAR analysis compared to the ECMWF background. Here we compare GPS/MET refractivity observations with various backgrounds from Data Assimilation Office (DAO) Data Assimilation System (DAS) forecasts. We retain the background with the best fit to GPS/MET refractivity. We perform 1DVAR analyses with the finite-volume DAO's DAS background and GPS/MET refractivity observations, and compare the results with nearby radiosondes.

[4] The outline of the paper is as follows: First we give a brief description of the GPS radio occultation technique and discuss the different possible approaches to retrieve and assimilate atmospheric properties from GPS measurements. Then, we describe the implementation of a 1DVAR analysis of refractivity. We then compare GPS/MET observed refractivity versus several backgrounds. After selecting the background which presents the smallest refractivity differences with the observations, we perform 1DVAR retrievals and compare them with nearby radiosondes. Finally, we attempt to interpret the 1DVAR analyses in the light of the refractivity differences between the background and the observations.

2. GPS Radio Occultation Technique

[5] This active remote sensing technique has already been discussed in great detail by, for example, *Kursinski et al.* [1997]. For the clarity of the work presented here, we briefly review the basic principles and advantages of the technique and the possible choices for assimilating the GPS observations.

2.1. Observables Collected During a GPS Occultation

[6] Rays from a source (GPS occulted transmitter) traverse the Earth's atmospheric limb to reach the LEO receiver. Since the two satellites are in relative motion, a Doppler shift is introduced in the received signal. An additional Doppler shift is introduced by the atmospheric and ionospheric refraction. After removal of the phase change due to the relative motion of the LEO with respect to the GPS transmitter, proper calibration of receiver and transmitter clocks, the extra phase change induced by the atmosphere and the ionosphere can be isolated.

[7] The overall refraction effect can be summed up by a total bending angle ε and an asymptotic ray-miss distance p (commonly called impact parameter) as shown in Figure 1. The uniqueness of the definition of the impact parameter assumes spherical symmetry, because in general the impact parameters at the entry and at the exit of the atmosphere are different. The vertical scanning of the atmosphere is provided by the relative motion between the two orbiting satellites. Time dependency of both ε and p can be derived from accurate measurements of Doppler-shifted frequency and precise knowledge of the time-dependent orbital geometry.

[8] A direct way to obtain the atmospheric refractive index profile n from ε and p is to use Abelian transformation assuming local spherical symmetry, i.e.:

$$n(x) = \exp\left[\frac{1}{\pi}\int_x^\infty \varepsilon(p)\left(p^2 - x^2\right)^{-\frac{1}{2}} dp\right], \qquad (1)$$

where $x = rn$ [e.g., *Fjeldbo et al.*, 1971].

[9] Errors in computing n by this approach were summarized by *Kursinski et al.* [1997]. They include contributions from (1) local spherical asymmetry [*Ahmad and Tyler*, 1999], (2) noncoplanar rays, (3) nonvertical scanning (because both satellites drift during an occultation [*Eyre*, 1994]) and (4) an inaccurate upper boundary used to initiate

the integral [*Steiner et al.*, 1999]. The integral formulation of the Abel transform spreads the errors in this boundary condition along the vertical.

[10] For microwave frequencies, after removal of the ionospheric contribution via the use of the two frequencies used by GPS for position determination [*Vorob'ev and Krasil'nikova*, 1994], the refractivity N (defined by $N = 10^6\ (n - 1)$) of the atmosphere can be expressed by:

$$N = b_1 \frac{P}{T} + b_2 \frac{P_w}{T^2}, \tag{2}$$

[e.g., *Smith and Weintraub*, 1953] where P is the pressure of air (dry air and water vapor) in hPa, T the temperature in K, P_w the partial pressure in water vapor in hPa, $b_1 = 77.6$ N-unit·K·hPa^{-1}, and $b_2 = 3.73 \times 10^5$ N-unit·K^2·hPa^{-1}.

[11] Refractivity profiles can be inverted into atmospheric temperature profiles, but this requires either using ancillary data (background or initial guess) or assuming that the contribution from the second term (sometimes referred to as "wet term") in equation (2) is negligible. In general, temperature (humidity) profiles can be retrieved provided humidity (temperature) data are available [*Kursinski et al.*, 1995].

2.2. Features of the GPS Radio Occultation Technique

[12] There are several interesting attributes of GPS occultations as an atmospheric sounding device. A high-inclination LEO receiver provides a set of observations that covers the globe fairly uniformly at a relatively low cost [*Yunck et al.*, 1988]. The homogeneity of the GPS coverage is advantageous for providing global observations in comparison to balloon-launched radiosondes (about 800 each 12 hours, the majority of which are over the Northern Hemisphere continents). A single GPS receiver can obtain approximately 500 occultations per day [*Kursinski et al.*, 1997]. This number assumes the GPS receiver can track both rising and setting occultations. It is less than the number of profiles obtained by a sounder on-board a meteorological polar-orbiting satellite. In order to collect more occultations per day, one must place more receivers into orbit, which is feasible because the receivers are simple and small.

[13] When compared within infra-red (IR) spaceborne sounders, the radio occultation (RO) technique with GPS has the advantage of being an "all-weather" system. Like microwave and unlike IR sounders, it is scarcely sensitive to aerosols and clouds. In addition, it is also insensitive to rain due to wavelengths of order 20 cm. Unlike most other techniques the GPS radio occultation provides a degree of self-calibration, because relative phase shifts are the relevant information. Moreover, the stability of the transmitter and receiver clocks limits temporal drifts.

[14] Finally, due to its limb-viewing geometry, the GPS RO has a higher vertical resolution (0.2–1.5 km) than passive nadir sounders [*Kursinski et al.*, 1997]. This vertical resolution is limited by Fresnel diffraction and is more comparable to radiosondes. Furthermore, the ratio between vertical and horizontal resolution (about 300 km) is consistent with that of quasi-geostrophic flows [*Lindzen and Fox-Rabinovitz*, 1989; *Kursinski et al.*, 1997].

2.3. Strategies for Data Assimilation

[15] There are several types of GPS RO data available for data assimilation [*Kuo et al.*, 2000]. Commonly, three have been considered so far: (1) bending angles [*Healy*, 1998; *Palmer*, 1998; *Matsumura et al.*, 1999; *Palmer et al.*, 2000; *Zou et al.*, 2000], (2) refractivity [*Zou et al.*, 1995; *Healy and Eyre*, 2000], and (3) retrieved profiles of temperature or water vapor [*Eyre*, 1994]. To be assimilated, each level requires an estimate of the errors and an observation operator along with its tangent linear model or adjoint [*Eyre et al.*, 1993]. The observation operator converts model state variables (i.e., temperature, humidity, pressure) into observed GPS data such as bending angles or refractivity.

[16] Briefly, bending angles have the simplest error correlations, but also have the most complicated and expensive observation operator. Conversely, retrieved temperature or humidity profiles have the simplest observation operator, but the most complicated error covariances. Assimilating refractivity represents a good alternative with a relatively low computing cost. A more extensive discussion of the various possibilities for assimilation of GPS data can be found in the work of *Kuo et al.* [2000].

[17] The approach chosen here is to retrieve both temperature and humidity in a one-dimensional (1D, in a vertical column) analysis based on a numerical weather prediction (NWP) model forecast background and refractivity measurements.

3. GPS-1DVAR Implementation

[18] We now describe the one-dimensional variational (1DVAR) analysis scheme and its components in detail.

3.1. Variational Theory

[19] The application of variational analysis to the retrieval of geophysical parameters has been discussed extensively by several authors [e.g., *Rodgers*, 1976; *Eyre et al.*, 1993]. We minimize a cost function $\mathcal{J}$ with respect to a state of atmosphere x (state vector). This function is

$$\mathcal{J}[x] = (h(x) - y^0)^T (O + F)^{-1} (h(x) - y^0) + (x - x^b)^T B^{-1} (x - x^b), \tag{3}$$

[e.g., *Jazwinski*, 1970] where y^0 is the observation vector, h is the observation operator (nonlinear), x^b is the background information (for example a 6-hour forecast), O, F, and B are the error covariance matrices of the observations, observation operator, and background, respectively. Hence $h(x)$ is an estimate of the observations that would be made with a state of the atmosphere x.

[20] The minimum variance problem can be solved using a quasi-Newton iteration, i.e.,

$$x_{i+1} = x^b + D_i^y \left(y^0 - h(x_i) + H_i (x_i - x^b)\right), \tag{4}$$

[e.g., *Rodgers*, 1976] where the subscript i denotes the iteration number, H_i is the tangent linear model of the observation operator h, or Jacobian, and D_i^y is the contribution function defined by

$$D_i^y = \left(H_i^T R^{-1} H_i + B^{-1}\right)^{-1} H_i^T R^{-1} \tag{5}$$

Table 1. Percentage of Occultations Penetrating the Troposphere Down to a Low Altitude in the GPS/MET 1995 June–July Data[a]

Lowest Point	North	Tropics	South
5 km or less	81	60	94
4 km or less	63	42	89
3 km or less	44	24	80
2 km or less	24	4	60
1 km or less	10	1	41

[a] "North" designates latitudes between 30°N and 90°N, "Tropics" 30°S–30°N and "South" 30°S–90°S. Values are in %.

[*Rodgers*, 1976] where $R = O + F$. We define convergence as the iteration at which the quantity $\mathcal{J}[x_i]$ has changed by less than 2% from the previous iteration, because further iterations did not make appreciable changes in the analysis. *Healy and Eyre* [2000] and *Palmer et al.* [2000] have found that the cost function at convergence can be used to quality control the GPS observations.

[21] After convergence, (4) represents a solution (the analysis) that has an optimal position or distance with respect to both the observations and the background provided that the background and observation errors are correct, unbiased, normally distributed, and uncorrelated with respect to each other. Since these postulates may not always be true, we may obtain a slightly suboptimal solution. A bias estimate is one way to address the problem [*Dee and da Silva*, 1998].

[22] Our state vector includes the temperature, the negative of the natural logarithm of the specific humidity at the background pressure levels, and the sea-level pressure. In the present implementation, the state vector extends to the lowest perigee point of the occultation.

3.2. The GPS Observations

[23] During the GPS/MET mission, there were four time periods when the Anti-Spoofing (A/S) encryption was turned off by the United States Department of Defense (USDoD). We used the same data set as [*Kursinski et al.*, 2000a], that is, "Prime Time 2" from 21 June to 4 July 1995. We chose this time period because the software then on the receiver enabled tracking the occultations deeper in the troposphere. Table 1 shows the percentage of occultations which probed the troposphere down to 5 km altitude or less. This number is higher in dry regions such as the Southern hemisphere (winter) than between 30°S and 30°N. The GPS data used here were processed by the Jet Propulsion Laboratory [*Hajj et al.*, 2002]. The locations of the 797 occultations of the data set are shown in Figure 2. No data were used for 24 June to 26 June 1995 because of problems with the GPS receiver.

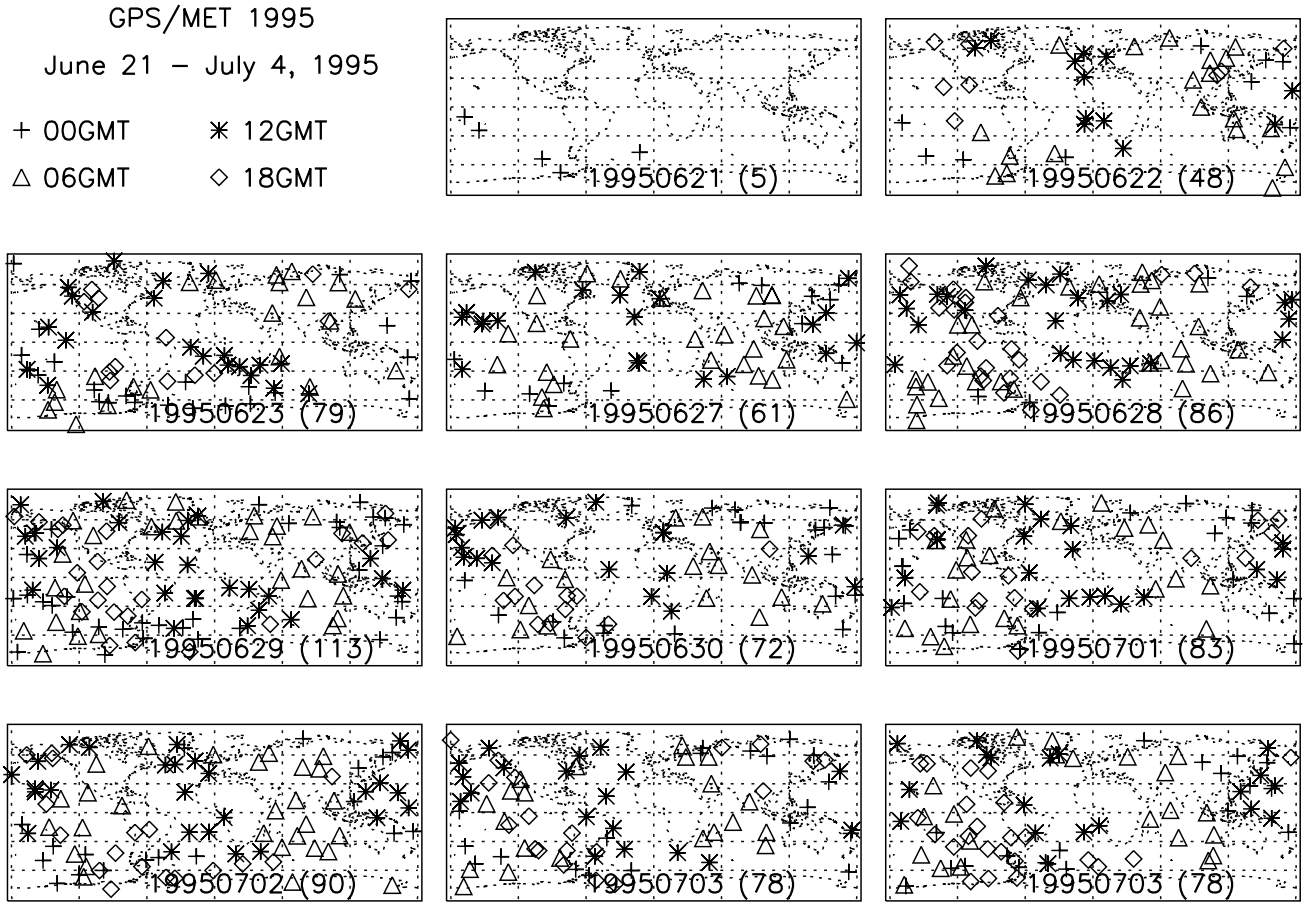

Figure 2. GPS/MET Occultations with no GPS encryption, June–July 1995. The chart is one map per day and the dates are shown at the bottom of each map, with the number of occultations for the day in parentheses. Different symbols are used for different synoptic periods.

[24] We assumed the following errors in the refractivity data: 1% below 5 km, 0.2% up to 30 km, based on the estimates of *Kursinski et al.* [1995, 1997]. Above 30 km, several sources of error, negligible in the troposphere, become gradually more important as the refractivity becomes very small [*Kursinski et al.*, 1997]. *Hocke* [1997] identified "wave-like structures" in the upper stratosphere in GPS retrieved temperatures. Since we cannot determine whether these are real or result from errors in the observations, we simply chose not to give weight to the GPS refractivity observations above 30 km, by assigning a 50% error in refractivity above that altitude in the present analysis.

[25] We incorporate inter-level observation error covariances using a Gaussian-type decrease:

$$Cov(N_i, N_j) = \sigma_{N_i}\sigma_{N_j} \exp\left(-\frac{(z_i - z_j)^2}{\Delta L_i \Delta L_j}\right), \quad (6)$$

where $Cov(N_i, N_j)$ expresses the refractivity error covariance between two levels i and j, σ_{N_i} is the refractivity standard deviation for the refractivity observation N_i. The correlation length ΔL_i depends on the spacing of the two levels surrounding the observation altitude z_i:

$$\Delta L_i = \frac{1}{4}(z_{i+1} - z_{i-1}). \quad (7)$$

This formulation was derived empirically and enables the observation error covariance matrix to remain positive definite even when the observations are very close (500 m vertical spacing or less).

3.3. The Observation Operator

[26] The observation operator converts temperature, humidity, and pressure profiles into refractivity profiles expressed as a function of altitude. It contains the physics of the measurement and an appropriate space-time interpolation. The background profile at the observation location is obtained by interpolating bilinearly between the model grid points. There is no temporal interpolation. It follows that (1) computing refractivity and (2) mapping pressure levels onto altimetric levels are the two main features of this operator. The observation operator can be represented by

$$h(x) = \mathcal{I}(\mathcal{F}(x)), \quad (8)$$

where $\mathcal{F}$ represents the application of equation (2) at each background level, and $\mathcal{I}$ is the interpolation operation.

[27] Instead of performing the analysis on the levels of the forecast, it is possible to work on more levels, for example the levels of the observations. Such an approach can yield analyzed profiles that account for the high resolution features detected by the GPS that cannot be represented by a relatively coarse analysis [*Kursinski et al.*, 2000a]. Because the profiles are to be assimilated in a global Data Assimilation System (DAS) we chose to work at the approximate vertical resolution of the DAS. Moreover, the computational cost of analyzing at model resolution is smaller because there are less levels in the background than in a typical GPS occultation (60–90 observation altitudes).

[28] There are two different ways of performing the forward operation: (1) computing refractivity at each model level, then interpolating the refractivity profile expressed in pressure levels into a profile expressed in altimetric levels; (2) interpolating model variables from each pressure level to the altitudes of the GPS observations, then computing at each point the refractivity value.

[29] Since calculating refractivity with interpolated values for temperature and water vapor content (choice (2)) makes the tangent linear model more complex, we chose to calculate refractivity first and to interpolate it after (choice (1)).

[30] Refractivity values are computed for each model level using equation (2). For each of these levels, the altimetric altitudes are calculated using a hydrostatic integration. Assuming the altitude at the sea-level pressure is 0 meter, the refractivity values are interpolated logarithmically to the altitudes of the observations.

3.4. Linearized Version of the Observation Operator

[31] In (4) we must have an observation operator h and its Jacobian H, the partial derivatives of the observation operator with respect to the elements of the state vector. We derived an analytical formulation for H. As a check, it was compared with a computation by finite differences as in the work of *Eyre et al.* [1993].

[32] The refractivity at one level is sensitive to a variation in temperature and humidity at that level and under that level. This is the result of the altitude calculation using hydrostatic integration starting from the surface. A change in the state vector at a given altitude has no influence on the simulated refractivities located below, but influences the altitudes of the pressure levels above, and hence the refractivity. Figure 3 shows a few columns of the H matrix.

[33] A positive perturbation in temperature corresponds to a decrease in refractivity at the same level. It has no influence on the calculated refractivities at lower altitudes. The value of the refractivity at each pressure level located above does not change. However, due to the increase in temperature and hydrostatic integration, all the pressure levels above are moved to higher altitudes. This shifts the upper part of the refractivity profile to higher altitudes, and increases refractivity for a given altitude.

[34] Increasing humidity increases the local refractivity (the plot is for $-\ln(q)$). This has very slight influence on other levels through the hydrostatic integration.

[35] The sea-level pressure has no direct influence on the refractivity values of each model pressure level. However, it increases the pressure difference between each model level and the sea level, which is the equivalent to increasing the altitudes. The final effect of a positive perturbation in sea-level pressure is hence to increase refractivity for a given altitude.

4. Model Comparison and Selection of the Background

[36] We define the innovation here as the difference between the refractivity calculated from the background minus the observed GPS refractivity. Since refractivity values span several orders of magnitude, we characterize the innovation in terms of percent of observed refractivity. We first calculate the refractivity innovations using different

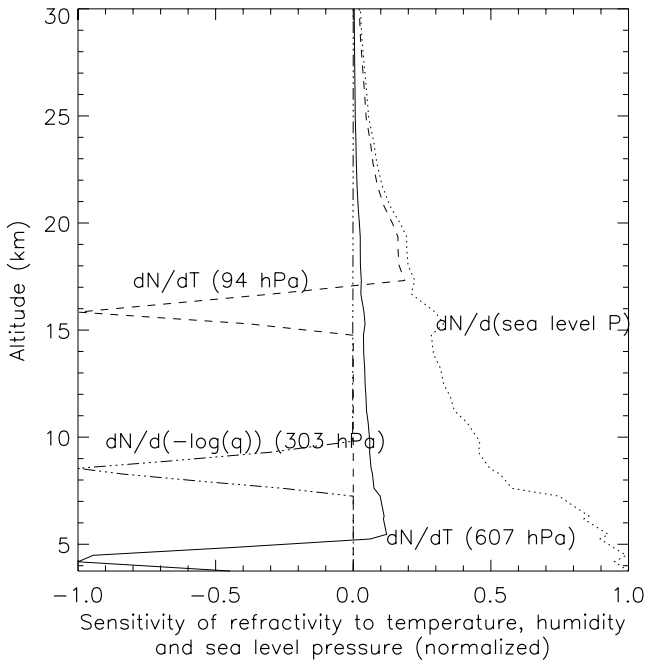

Figure 3. Jacobian for the GPS 1DVAR. The curves show derivatives of the observation operator with respect to temperature at 607 and 94 hPa, humidity at 303 hPa, and sea-level pressure. The observation operator simulates refractivity for an occultation which occurred on 29 June 1995 at 0218 GMT, located at 7°N and 128°E. No refractivity observations were simulated below 3.7 km altitude for this occultation because no data were reported.

backgrounds. These refractivity differences, or innovations, are shown in Figure 4.

[37] The first background (GEOS) was from the 1995 DAO DAS. We also use two backgrounds from the DAO's next-generation finite volume DAS; one background assimilates NESDIS TOVS temperature retrievals, whereas the other (DAOTOVS) uses radiances via a 1DVAR approach. The horizontal resolution is the same for the three backgrounds (2 × 2.5 degrees).

4.1. GEOS Background: Forecast and Assimilation

4.1.1. GEOS System Characteristics

[38] We first used background information from the Goddard Earth Observing System (GEOS) Data Assimilation System (DAS) version 1+ for our analysis [*Takacs et al.*, 1994; *Schubert et al.*, 1995]. It included more upper stratospheric levels than the GEOS-1 DAS used for a 15-year reanalysis. Since the 6-hour forecast was only archived on 18 selected pressure levels (surface to 0.4 hPa), we used a product called the "assimilation" for the background. The assimilation is available on the 46 σ levels of the General Circulation Model (GCM) from the surface to 0.1 hPa.

[39] The Data Assimilation Office (DAO) GEOS-DAS version 1 uses an Incremental Analysis Update approach [*Bloom et al.*, 1996] in an Optimal Interpolation framework [*Pfaendtner et al.*, 1995]. It consists of applying gradual analysis increments to the model integration within the 6-hour assimilation window. The "assimilation" is the result of this operation in the middle of the window. So this second set of background information already contained some information from the observations available during the assimilation period, especially radiosondes (RS).

[40] A first study showed that the 1DVAR retrievals are sensitive to the number of levels used for the analysis. The limited number of levels for the GEOS Forecast (only 18 levels) is insufficient in order to capture the full structures that a 1DVAR could resolve with 46 levels, especially near the tropopause [*Poli et al.*, 2001]. We show here the innovations using the GEOS Assimilation as the background.

4.1.2. Comparison With GPS/MET Refractivity

[41] In the North (average of all profiles at latitude above 30°N), we can see from Figure 4a that the GEOS background refractivity presents a positive bias with respect to the GPS/MET refractivity, except between 7 and 10 km. The standard deviation of innovation in Figure 4d decreases from about 3% around 2 km altitude down to less than 1% between 7 and 30 km altitude. Below 5 km, the innovation standard deviation grows significantly, indicating contributions from some combination of (1) errors in the background information, (2) errors in the measurements, and (3) observation operator errors including phenomena such as multipath that are not simulated correctly.

[42] In the Tropics, we can identify similar features: The mean innovation (Figure 4b) between 1 and 30 km altitude is positive except between 12 and 17 km. The standard deviation in Figure 4e grows more rapidly than in the North when approaching the surface: 3% at 5 km altitude instead of 2% in the North at the same altitude, maximum of 5.3% at 2 km altitude (note only 12 comparisons for this altitude).

[43] In the South, the innovation bias in Figure 4c is similar to the North, i.e., positive up to 8 km altitude and then negative up to 12 km altitude. However, the bias becomes negative again above 25 km altitude. The standard deviations (Figure 4f) are higher than in North above 8 km altitude. This suggests that the GEOS Assimilation is more accurate at these altitudes in the North where it is more constrained by RS than in the South. Below 8 km, the lower standard deviation in the South is perhaps related to the humidity. Since the GPS/MET measurements are in the boreal Summer, the winter Southern hemisphere has a lower mean specific humidity. This implies that the humidity contributes more to the refractivity observations in the North than in the South. And since the *temperature* forecasts are generally better in the North than in the South, this suggests *humidity* as a source of difference.

4.2. FVDAS Background: 6-Hour Forecasts After Assimilation of NESDIS TOVS

4.2.1. FVDAS NESDIS TOVS System Characteristics

[44] The Finite-Volume DAS (FVDAS) [*DAO*, 2000] uses a global three-dimensional Physical-space Statistical Analysis System (PSAS) assimilation scheme [*Cohn et al.*, 1998] and the NASA/NCAR (National Aeronautics and Space Administration/National Center for Atmospheric Research) Finite Volume General Circulation Model (GCM). The GCM has 55 levels between the surface and 0.01 hPa. One significant feature of the FVDAS resides in the dynamical core of the GCM which uses a Lagrangian vertical coordinate system [*Lin*, 1997]. To initialize the

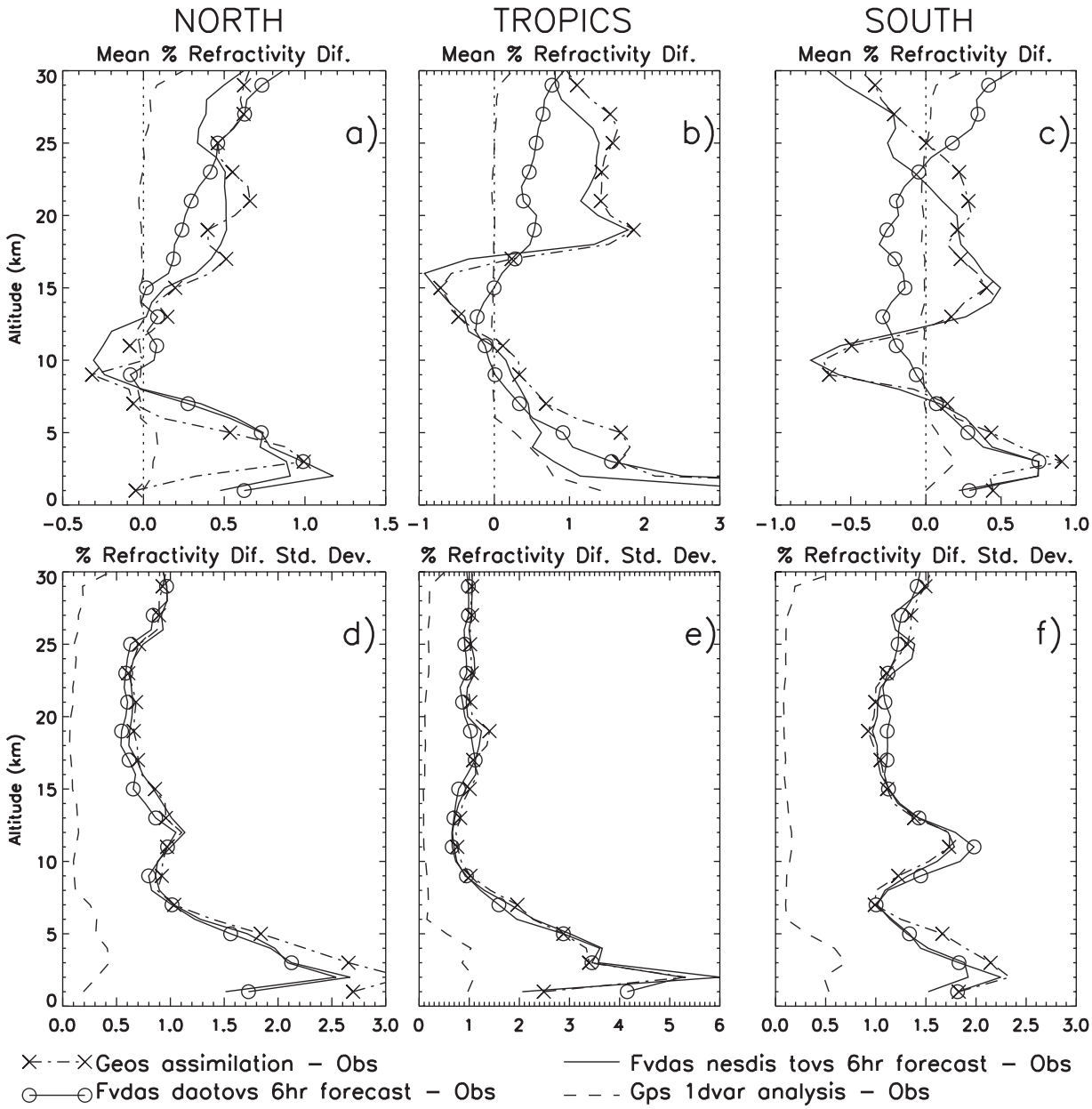

Figure 4. Refractivity differences with GPS/MET observed refractivity for three different backgrounds and the GPS 1DVAR analysis. All quantities in percents of observed refractivity. Number of profiles: 277/274/223 for North/Tropics/South, respectively.

model we used Atmospheric Model Intercomparison Project (AMIP) climatological "cold" runs, with a spin-up of 3 weeks by assimilation of the observations (mainly RS and TOVS) before the beginning of the time period for which we had GPS/MET data. The FVDAS background information used in this study is interpolated to the same 46 σ levels as the GEOS Assimilation.

[45] One important source of observations for the DAS comes from the TIROS Operational Vertical Sounder (TOVS) soundings. The National Oceanic and Atmospheric Administration (NOAA) National Environmental Satellite, Data, and Information Service (NESDIS) provides operational profiles of retrieved temperature. These profiles are obtained via a retrieval method using a radiosonde-based background rather than a short-term GCM forecast [*Reale et al.*, 1994]. We refer to the 6-hour forecasts issued by this system as "FVDAS NESDIS TOVS" hereafter.

4.2.2. Comparison With GPS/MET Refractivity

[46] From Figure 4a, we can see that in the North the FVDAS NESDIS TOVS background refractivity bias has about the same shape as the GEOS Assimilation. The negative region has been shifted upwards (8–12 km instead of 7–10 km). Also, the bias curve looks smoother than the GEOS, i.e., less wave structures between 15 and 25 km altitude. A significant difference resides in the standard deviation shown in Figure 4d. It has been decreased by an amount of up to about 1% below 6 km altitude when compared with the GEOS Assimilation.

[47] In the Tropics, the bias in Figure 4b has been shifted toward more negative values, thus making the average innovations over the profile closer to zero.

[48] Bias and standard deviation results in the South are very similar to the GEOS Assimilation results in Figures 4c and 4f.

4.3. FVDAS Background: 6-Hour Forecasts After Assimilation of DAOTOVS

4.3.1. Differences Between NESDIS TOVS and DAOTOVS

[49] The "FVDAS DAOTOVS" background assimilates TOVS observations in the FVDAS via the assimilation of DAOTOVS temperature and humidity interactive retrievals, instead of the assimilation of NESDIS temperature retrievals. The DAOTOVS system relies on a 1DVAR cloud-clearing embedded in the assimilation cycle. It uses the latest available 6-hour forecast as a background to initiate the 1DVAR retrievals and includes a Kalman-filtered radiance bias correction based on RS [*Joiner and Rokke*, 2000].

4.3.2. Comparison With GPS/MET Refractivity

[50] In the North the FVDAS DAOTOVS innovation bias shown in Figure 4a does not exhibit significant negative values in contrast to the other two backgrounds. The crescent shape of the curve is conserved, though, but with reduced waviness between 15 and 25 km altitude. The standard deviation in Figure 4d is smaller than the GEOS Assimilation and FVDAS NESDIS TOVS above 3 km altitude. One explanation for this reduction in standard deviation could be that some phenomena observed by the GPS have been captured by the FVDAS DAOTOVS 6-hour forecast, but not by the two other backgrounds.

[51] A major difference is observed in the Tropics, where the innovation bias in Figure 4b is now confined between −0.5% and 1% above 5 km altitude, whereas before these extrema were −1% and 2% for the other two backgrounds. This significant reduction of bias, associated with no real change in standard deviation in Figure 4e, is another indication of the improvement of the system from NESDIS TOVS to DAOTOVS. It is interesting to notice that a change in the origin of the TOVS data can drastically change the innovation bias curve. This change is not detected in the North, but is much more striking in the Tropics where fewer RS are available to constrain the climatology of the model-analysis.

[52] We also observe a major difference in the South. The innovation bias in Figure 4c has been significantly reduced as compared with FVDAS NESDIS TOVS and GEOS Assimilation. The climatology of the model-analysis, that we can examine using an independent refractivity data set (GPS/MET), has changed dramatically: The bias has generally been reduced, assuming the GPS/MET observations are nonbiased. As in the Tropics, this shows that the TOVS data strongly drive the model-analysis climatology in the Southern hemisphere where only very few RS observations are available. However, in contrast to the general results, the standard deviations in the South in Figure 4f have slightly increased above 8 km altitude compared to the FVDAS NESDIS TOVS. We are currently investigating the source of this result. It might be due to an insufficient spin-up of the FVDAS DAOTOVS system.

4.4. Selection of the Background

[53] To summarize, smaller refractivity innovations are observed with the FVDAS DAOTOVS than the other backgrounds in the North and the Tropics. We therefore use the FVDAS DAOTOVS background in the rest of the paper.

[54] As an independent check, a comparison of the temperature profiles from the three backgrounds with nearby RS yielded the same result: The GEOS Assimilation and FVDAS NESDIS TOVS have comparable climatologies (assuming those are measured by the bias), the FVDAS DAOTOVS has smaller biases globally and reduced standard deviations in the North [*Poli et al.*, 2001]. The agreement between the two studies suggests that GPS refractivity can be used as an independent data set for model validation studies.

4.5. Background Error Covariance Matrix

[55] The background error covariance matrix uses variances derived by comparison of the FVDAS DAOTOVS 6-hour forecasts with nearby radiosondes. For temperature, the covariances includes inter-level correlations through the following formula:

$$Cov(T_i, T_j) = \sigma_{T_i}\sigma_{T_j} \exp\left(-\left(\frac{\ln(P_i/P_j)}{\Delta L}\right)^2\right)\exp\left(-\left(\frac{T_i - Tj}{\Delta T}\right)^2\right), \quad (9)$$

where $Cov(T_i, T_j)$ expresses the temperature error covariance between two levels i and j, σ_{Ti} is the temperature error standard deviation for the pressure level P_i, T_i is the temperature at that level, $\Delta L = 0.1$, and $\Delta T = 3\ K$ are constants which were experimentally adjusted. Using this formulation, two levels close in natural logarithm of pressure and temperature have highly correlated errors. In order to account for the variable altitude of the tropopause, we specify the local maximum of model error to occur at the altitude of the temperature minimum. Figure 5 shows the square root of the diagonal of the background error covariance matrix for temperature.

[56] For humidity, we assumed errors shown in Table 2. Those errors were derived in the same manner as the assumed background temperature errors. For the humidity inter-level correlation error only the term representing the exponential decrease related to the vertical distance between two levels in (9) is taken into account.

[57] We assume a sea-level pressure error standard deviation of 2.5 hPa. We neglect cross-correlations between the different variable types in the background (temperature, humidity, and sea-level pressure).

5. Comparisons With Radiosondes

[58] In this section we compare results of GPS 1DVAR analyses with nearby radiosondes (RS), and discuss the statistics obtained.

5.1. Radiosonde Matches

[59] The matching criteria are ±3 hours in time and less than 280 km in distance. The GPS temperature (humidity) direct retrievals obtained using an estimate of humidity (temperature) [*Hajj et al.*, 2002] are also shown, as well as the background used to perform the 1DVAR analysis.

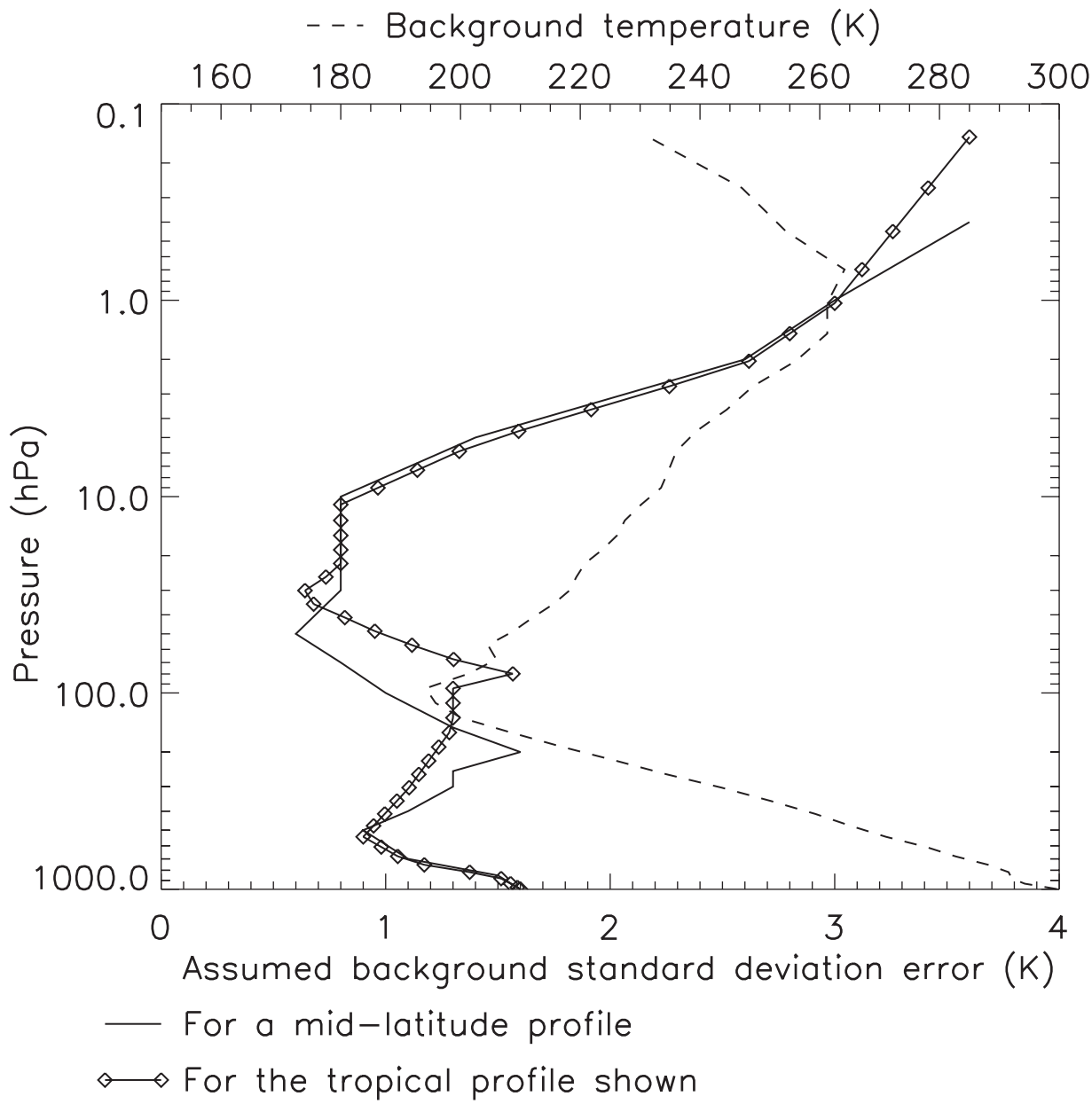

Figure 5. Assumed background temperature errors.

[60] Among the 797 GPS occultations, 102 match the collocation criteria in the North (31 and 10 in the Tropics and the South, respectively). Since most of the matches occur in the Northern hemisphere, we will focus on this region. Only one 1DVAR minimization process did not converge. As a background check, collocations with discrepancies more than 5 K between background and RS are removed from the statistics. Typical RS temperature errors range from 0.5 K to about 1 K in the troposphere and increase to as large as 4 K at 10 hPa [*Rocken et al.*, 1997]. It is also necessary to apply some quality control to the GPS direct retrievals. Therefore, we also remove discrepancies more than 5 K between the RS and the GPS direct retrieval. No quality control is performed on the 1DVAR analyses. Likewise, all specific humidity differences (background minus RS or RS minus direct retrieval) greater than 100% are removed.

5.2. Temperature

[61] Figure 6 shows a single temperature profile which exhibits the advantages of combining information from a

Table 2. Assumed Natural Logarithm of Specific Humidity Errors for the Background

Pressure, hPa	Ln(q) SD
Less than 150	0.70
200	0.60
250	0.45
300	0.44
400	0.42
500	0.40
700	0.32
850	0.25
1000	0.20

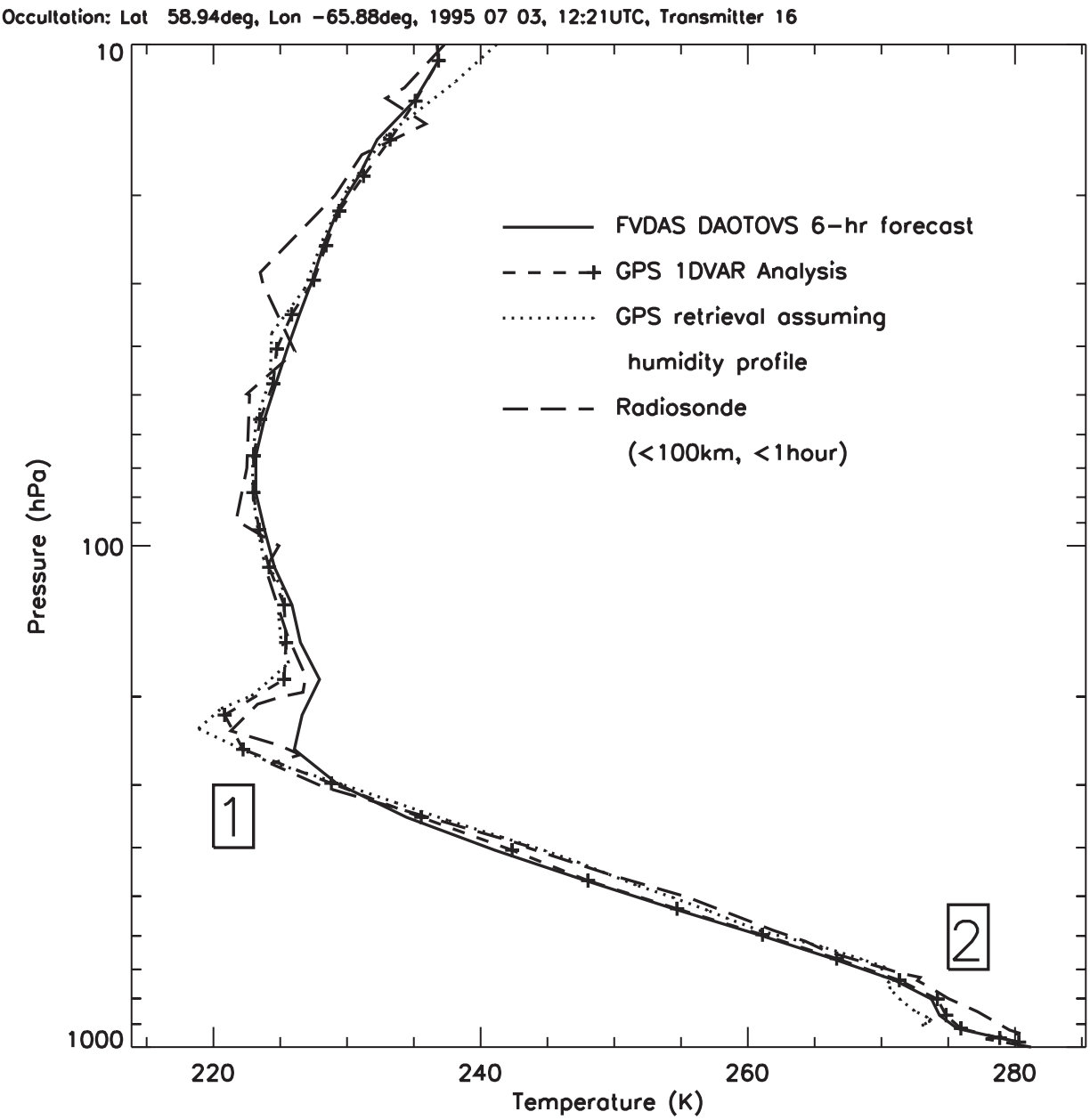

Figure 6. Temperature profile showing the advantages of using a variational approach with GPS data. See text for explanation of regions (1) and (2).

background and observations. (1) Both the direct retrieval and 1DVAR analysis are able to improve the tropopause as compared with the FVDAS DAOTOVS 6-hour forecast background. The background has a warm bias at the tropopause of about 5 K. (2) In the lowest layers, the 1DVAR analysis follows the background, whereas the direct retrieval diverges from the RS.

[62] Figure 7 shows the bias and standard deviation difference from nearby radiosondes for temperature in the Northern hemisphere (North of 30°N) and the number of data used to calculate each point. That number decreases toward the surface because many occultations during this time period did not reach the surface as shown in Table 1. Balloon bursts above the tropopause explain the decreasing number of comparisons in the stratosphere.

[63] All biases in Figure 7a (background minus RS, GPS 1DVAR analysis minus RS, direct retrieval minus RS) are of the order of 1 K or less below the 40-hPa level. The forecast and 1DVAR analysis have biases less than 0.5 K between 300 and 20 hPa. The direct retrieval presents a larger (negative) bias than the GPS 1DVAR analysis above the 400-hPa level. Above 100 hPa, the negative bias of the direct retrieval is consistent with the results of *Leroy* [1997] for the same time period (Summer 1995). He observed a negative bias in the geopotential height derived from GPS as compared to ECMWF forecasts, which are tightly constrained by radiosondes in the Northern hemisphere.

[64] The direct retrievals minus RS produce the largest standard deviations in Figure 7b below 400 and 850 hPa (2.4 K at 850 hPa). The FVDAS DAOTOVS minus RS

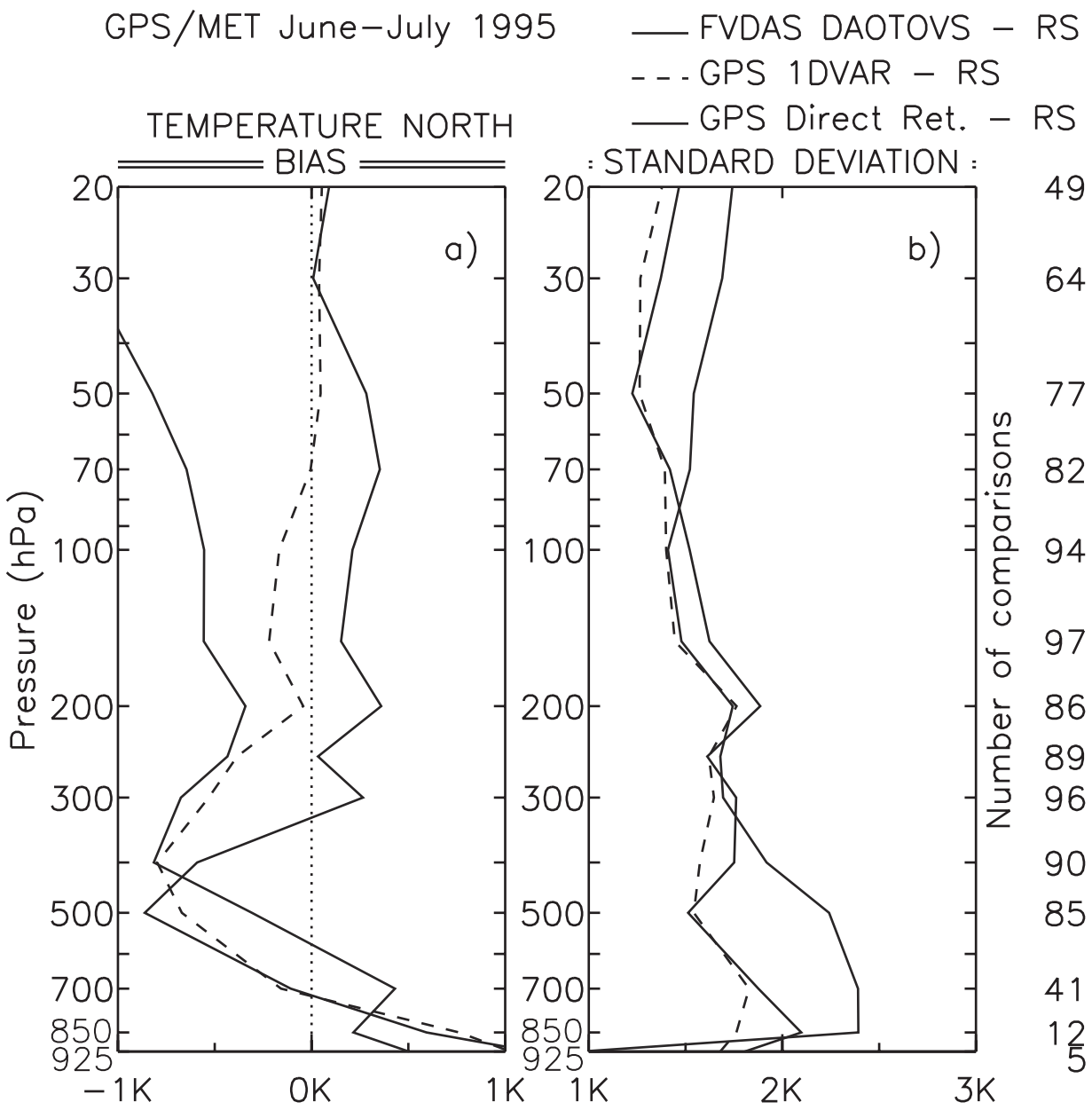

Figure 7. Northern Hemisphere, comparisons with radiosondes temperatures (± 3 hours, less than 280 km).

temperature standard deviations are less than 2 K between 700 and 20 hPa. The improvement of the 1DVAR analysis between 925 and 20 hPa (except at 500 and 50 hPa) over the background (by comparison with the nearby RS) suggests a better description of the tropospheric and lower stratospheric temperatures.

5.3. Humidity

[65] Figure 8a shows humidity bias with respect to nearby RS for the global domain. The FVDAS DAOTOVS 6-hour forecast background presents a bias less than 5.5% over the entire vertical range of the profile. The direct retrieval has a comparable bias in the 850- to 750- and 600- to 400-hPa regions. The 1DVAR bias is the largest (negative), except at 925 and 650 hPa. *Kursinski and Hajj* [2001] also found a negative bias in their humidity retrievals from GPS/MET refractivity.

[66] Figure 8b shows that the FVDAS DAOTOVS is the closest to the RS point measurements in terms of standard deviation between 850 and 700 hPa, with an increase from 30% at 925 hPa to about 45% at 450 hPa. The direct retrieval presents the largest standard deviation, except at 925 hPa. The 1DVAR standard deviation is the smallest in the 550- to 400-hPa region. However, the 1DVAR shows a slight degradation compared to the background below the 700-hPa level.

[67] Many radiosondes we used either did not report the humidity, or the reported humidity was different from the background and/or the direct retrieval by more than 100%. This results in a small number of comparisons. There are

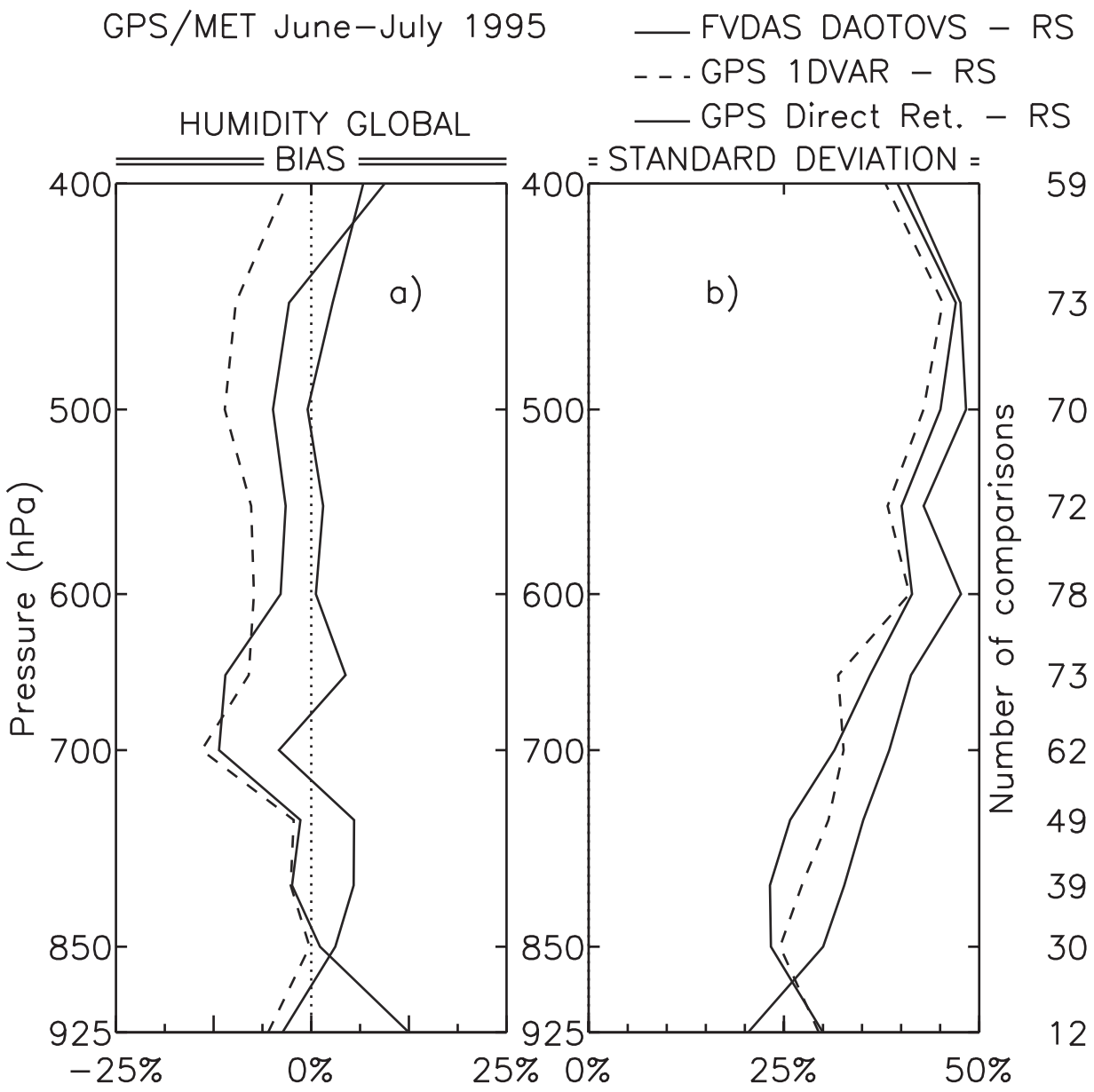

Figure 8. Comparisons with radiosondes (RS) humidity, average for the whole domain North/Tropics/South.

known problems with RS humidity measurements [e.g., *Soden and Lanzante*, 1996]. It is also known that humidity varies more over smaller scales than does temperature. In addition, the GPS observations average the refractivity over a long horizontal path whereas RS are more like point measurements. Clearly, the representativeness problem which arises from the humidity comparison performed here needs to be addressed in the future. We will discuss the humidity results in more detail later in the paper.

5.4. Sea-Level Pressure

[68] The sea-level pressure (SLP) is part of the state vector in the 1DVAR analysis. Table 3 shows that in the North and in the Tropics the 1DVAR analysis SLP has both higher bias and standard deviation than the background, when compared with RS. On the one hand, the SLP increments (i.e., 1DVAR analysis minus background) are needed to fit the background to the observed refractivity. Without these increments, investigations have shown that the adjustment occurs in temperature, and the comparisons with the RS are degraded [*Poli et al.*, 2001]. But on the other hand, we can see from the Table 3 that these SLP increments do not agree with the SLP reported by RS.

[69] We discuss the origin of these SLP increments and the implications for the use of SLP derived from GPS radio occultations into NWP in the next section.

6. 1DVAR Interpretation of the Refractivity: The Increments

[70] In order to gain some insight into the way the 1DVAR creates increments in temperature, humidity and

Table 3. Sea-Level Pressure Statistics for Profiles With Nearby RS

Geographic Area	North (102 Cases)		Tropics (31 Cases)	
Sea-level pressure, hPa	Mean	SD	Mean	SD
Background minus RS	0.0	2.6	−0.7	1.4
1DVAR analysis minus RS	−1.3	4.9	−3.8	3.6
Increment	−1.3	4.1	−3.1	3.5

sea-level pressure, we now discuss how the minimization of refractivity differences between the background and the observations performed by the 1DVAR relates to the analysis increments.

6.1. Residuals

[71] The residual is defined here as the difference between the 1DVAR refractivity and the GPS observations. The curve "1DVAR analysis" in Figure 4 shows these residuals. As expected, the 1DVAR has succeeded in pushing the solution refractivity much closer to the GPS/MET observation than the background refractivity (curve "FVDAS DAOTOVS"). However, in the 1DVAR theory, we assume that both observations and the background errors are Gaussian and not biased. Figures 4a, 4b, and 4c show that these assumptions are not met, i.e., there are biases. An interesting point is that the 1DVAR removed some of the bias: The bias of the 1DVAR refractivity residual is close to zero. However, if we look carefully, bias remains in the residuals. This is most apparent near the surface in the Tropics where the background bias was the strongest. For example, a separate bias correction such as discussed and presented by *Dee and Todling* [2000] is necessary to fully account for these biases.

[72] The refractivity differences in Figure 4e were reduced to 1% in standard deviation in the Tropics, which is consistent with the 1% refractivity error assumed below 5 km altitude. However, in the Northern and Southern hemispheres in Figures 4d and 4f, refractivity residuals below 5 km altitude are approximately 0.4–0.6% which is smaller than the errors assumed. Errors in the residuals combine errors from both the analysis and the measurement. They hence represent an upper limit on the real value of the measurement error. Consequently, the low values in residual standard deviation suggest the 1% refractivity error estimates of *Kursinski et al.* [1995, 1997] may be too large in those regions.

[73] In the present attempt to estimate the refractivity errors characteristics from the residuals for further assimilation studies, we now consider the refractivity residuals vertical correlations. They are shown in Figure 9. The figure also shows the innovation vertical correlations (curve "Background"). Those correlations are broader than the residuals vertical correlations (curve "1DVAR analysis"). The former include error structures from the background and we cannot separate the background error vertical structures and the GPS intrinsic error structures. The residuals represent a closer representation of the GPS vertical structures, even though they have of course retained some memory of the background error.

[74] The vertical correlations in the 1DVAR results are closer to exponential decays than the Gaussian decays assumed in the construction of the observation error covariance matrix. A least squares statistical fit showed that those correlations functions had correlation lengths between 1 and 3 km, while the background refractivity errors have larger vertical correlations lengths between 2 and 7 km in the North and in the Tropics, and between 8 and 12 km in the South. Changing the correlations in the observation error covariance to values similar to the ones found here did not change significantly the results shown in the paper.

6.2. Sea-Level Pressure Increments

[75] We begin with the sea-level pressure (SLP) since it is the most straightforward to interpret. A SLP shift is somewhat equivalent to a height shift, which itself translates into a fractional refractivity shift: We can approximate the refractivity as varying with a constant scale height H, i.e.

$$N = N_0 \exp^{-\frac{z}{H}}. \tag{10}$$

Then the fractional variation in refractivity at any altitude due to a given height shift Δz is approximately

$$\frac{\Delta N}{N} \approx -\frac{\Delta z}{H}. \tag{11}$$

[76] From (11) we can predict qualitatively how the 1DVAR analysis modifies the background sea-level pressure, given an observed and a background refractivity profile. In the North, Figure 4a shows that the background refractivity is higher in the mean than the observations. This is seen by integrating the area between the zero-mean vertical axis and the innovation curve (FVDAS DAOTOVS background minus observation). To correct for this positive background minus observation refractivity mean difference in the North, the 1DVAR analysis creates a negative mean SLP increment in this region, which is consistent with the result of Table 3. Likewise, the mean SLP increment is negative in the Tropics, but with a greater SLP mean increment (−3.1 hPa instead of −1.3 hPa in the North) corresponding to a greater area between the zero-mean vertical axis and the innovation curve for this geographical area in Figure 4b.

[77] Visually, Figure 10 shows the transition, in the North, from the "FVDAS DAOTOVS" mean curve, representing refractivity residual calculated with the background SLP, to the "1DVAR SLP" mean curve, representing background refractivity calculated with the 1DVAR SLP. As expected, we can see that the 1DVAR SLP mean curve in Figure 10a has been shifted toward more negative values, thus making the integrated area between it and the zero-mean axis now closer to zero. Consequently, the negative refractivity bias observed previously between 7 and 10 km is even more negative.

[78] Figure 10b shows a reduction in standard deviation when going from the residual to the 1DVAR SLP curve. This suggests that valuable information in terms of height shift between the background and the GPS observations may be contained in the GPS refractivity measurements. It is not completely clear though whether this height shift relates to the first order to an incorrect sea-level pressure in the background or if it is primarily due to other sources of

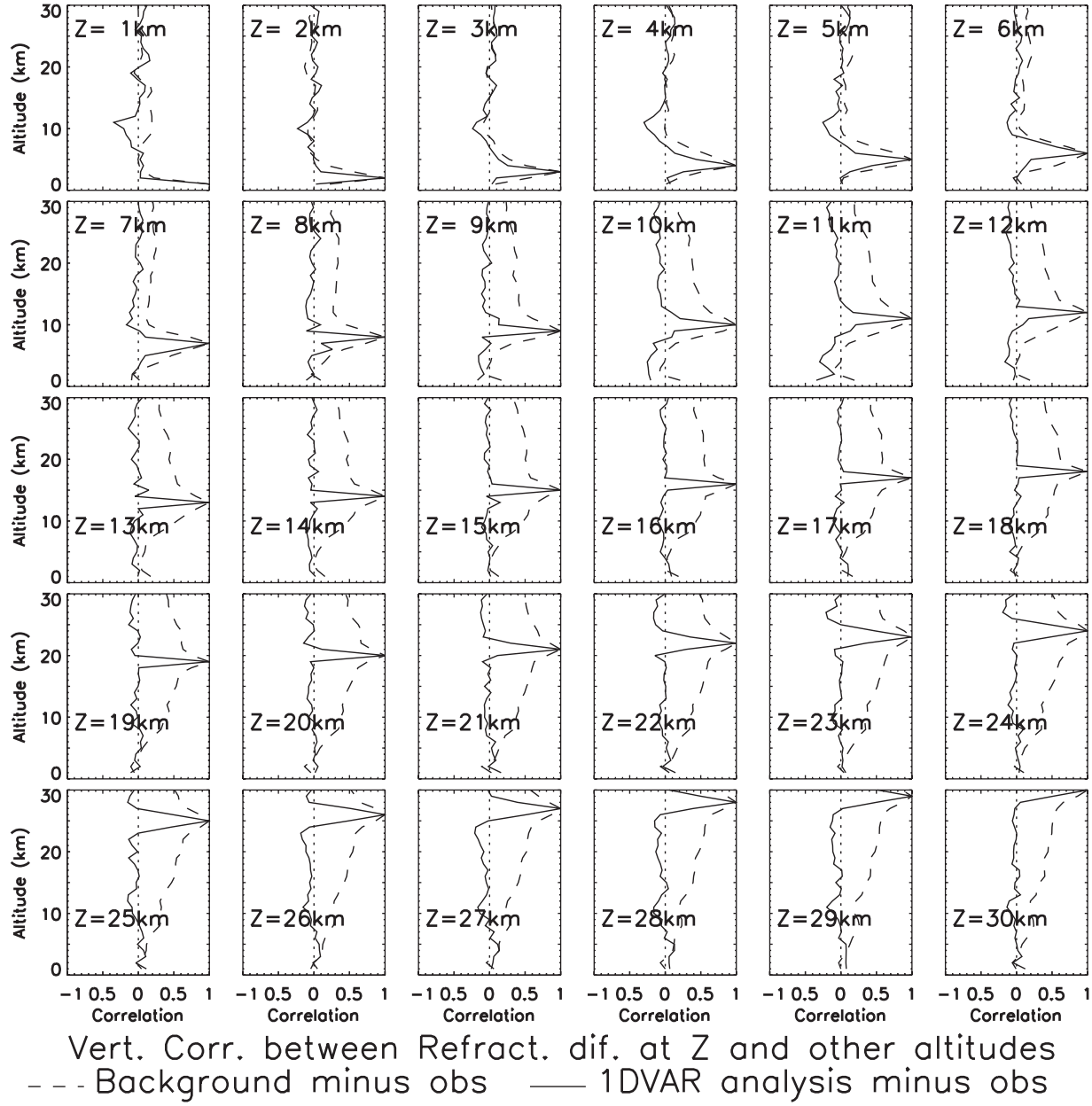

Figure 9. Vertical correlations at various altitudes, for all the refractivity profiles.

error that could be contained either in the measurements or in the observation operator.

[79] *Palmer and Barnett* [2001] developed an optimal estimation inverse method based on ECMWF background and GPS/MET bending angles and found consistent results, i.e., negative surface pressure increments on a global average. However, they found positive increments in the Tropics. A possible explanation for this difference might be the number of points used to compute the statistics in the Tropics (9 instead of 31 in the present paper).

[80] It is indeed possible that a discrepancy exists between the references used in the processing of the GPS data and the reference used in the model used as a background (i.e., different geoids). Also, another source of difference might be the spherical symmetry assumption made when deriving the impact parameter (and thus the altitude) of the tangent points from the bending angle measurements.

[81] In any case, these discrepancies require further attention before using surface or sea-level pressures derived from GPS radio occultation in a weather and/or climate model.

6.3. Temperature Increments

[82] Figure 11 shows the 1DVAR temperature increments as a function of pressure and altitude. The right axis (altitude) in Figure 11b is based on the US Standard Atmosphere 1976 [*NOAA*, 1976]. The largest mean increments in Figure 11a are in the upper troposphere near the tropopause in the [30°S–30°N] region. The mean temper-

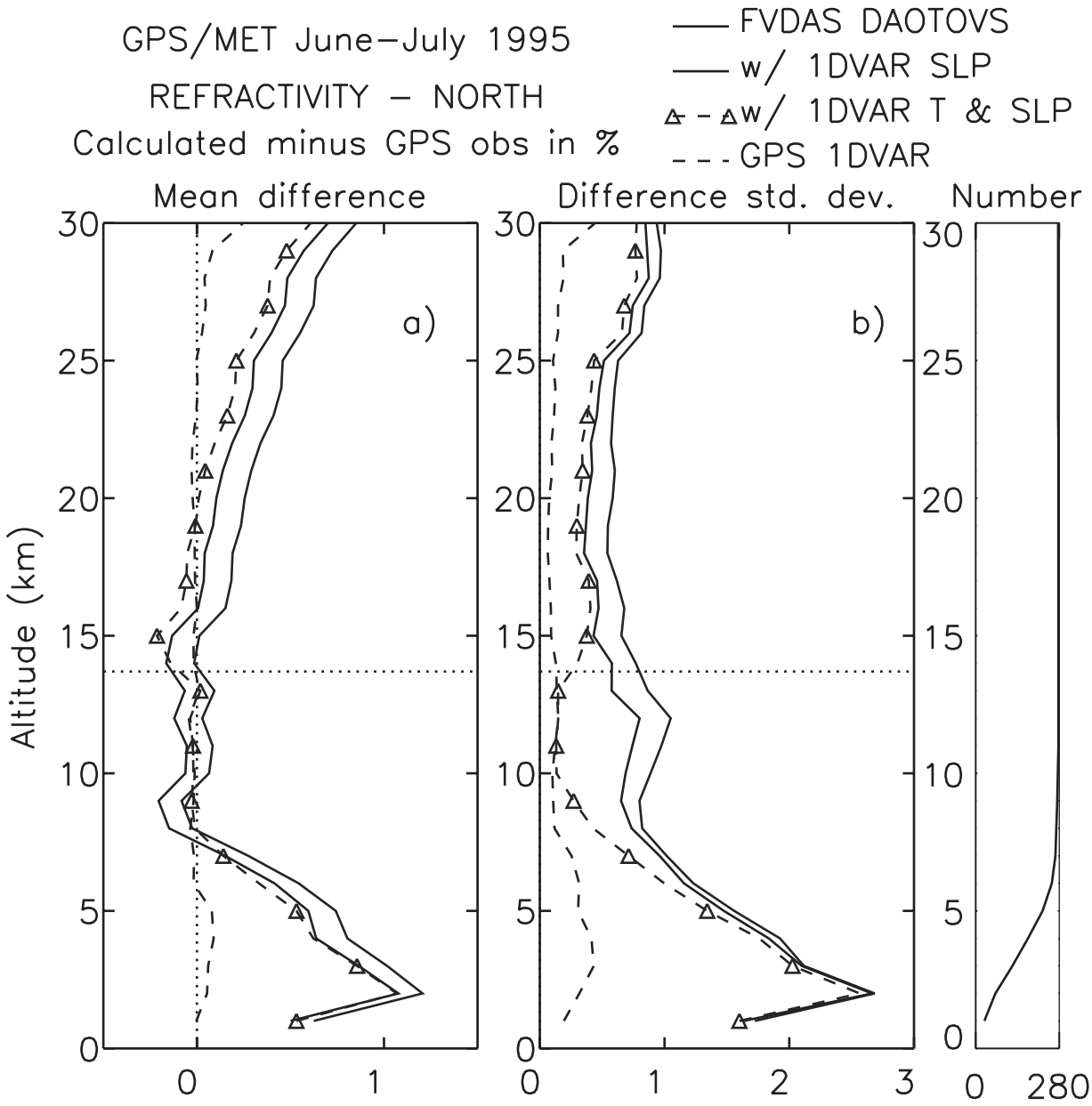

Figure 10. Refractivity differences with observations for various combinations of simulated refractivity. See text for the details of each curve.

ature increments are less than 0.6 K (0.9 K) in the North region ([30°S–30°N], respectively). They exhibit a dipole behavior: They are usually positive below the region 400–300 hPa, and negative above. Below the 400-hPa level, the positive increments in the North are consistent with the negative temperature bias in the FVDAS background in the same region, based on the RS comparisons shown previously. The usually negative increments in the upper troposphere and lower stratosphere are consistent with the findings of *Palmer and Barnett* [2001]. They suggest that the background is too warm in this region, especially in the latitudes [30°S, 30°N].

[83] We now examine the temperature increment contribution to the transition from innovation to residual. Temperature has two effects on the refractivity: a local effect (see equation (2)) and a nonlocal hydrostatic effect. Including increments in an isolated part of the temperature profile enables us to gauge the influence of the hydrostatic effect in fitting the observations. The "1DVAR T & SLP" curve (noted 1DVAR T_SLP in the rest of the paper) in Figure 10 uses 1DVAR SLP and 1DVAR temperatures from the surface to the 150-hPa level (about 14 km altitude). No temperature increments are used to generate this curve above 14 km altitude. We now examine the difference between the 1DVAR SLP curve and the 1DVAR T_SLP curve and attempt to relate this transition to the 1DVAR temperature increments in Figure 11.

[84] Below 6 km altitude, the positive mean temperature increments in Figure 11a help slightly reduce in the same region the positive innovation bias in Figure 10a between

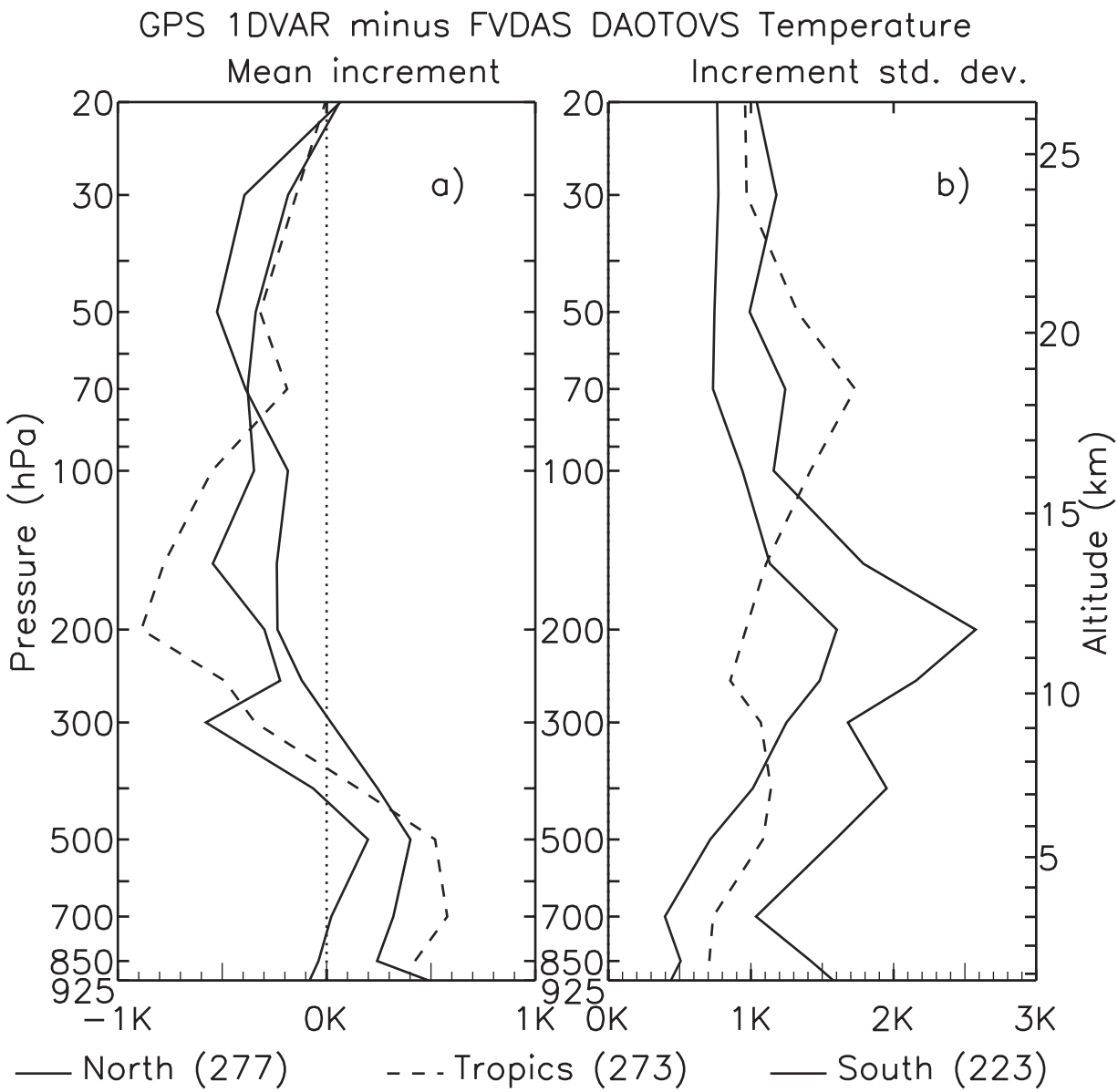

Figure 11. GPS 1DVAR analysis minus FVDAS DAOTOVS background temperature (increments). The number of profiles for each geographic area (North, Tropics, South) is shown in parentheses in the legend.

the 1DVAR SLP and 1DVAR T_SLP mean curves. We also observe a small reduction of standard deviation innovation in Figure 10b at the same altitudes. Between 6 and 14 km, the 1DVAR T_SLP standard deviation is significantly lower than the 1DVAR SLP.

[85] Above the cutoff altitude at about 14 km, we should not see any local temperature effect provided the temperature has not changed from the background, but we do see the hydrostatic effect of the negative temperature increments applied below the cutoff. The increments have compressed the atmosphere between 6 and 14 km, thus lowering the atmosphere located above. As a consequence, the mean refractivity difference with the observations has been reduced in Figure 10a. We note that this hydrostatic adjustment to the refractivity above 14 km is close in magnitude to the modifications due to the SLP change. This suggests that a temperature bias in the background might cause the 1DVAR to erroneously change the SLP instead of producing a larger increment in temperature.

[86] In order to bring the remaining refractivity differences in the 1DVAR T_SLP curve closer to a zero mean above 14 km altitude in Figure 10a, the 1DVAR has generally created negative temperature increments. The 1DVAR T_SLP curve is transformed into the ''GPS 1DVAR'' curve above 14 km altitude by applying in this region the temperature increments.

6.4. Humidity Increments

[87] With the SLP and the temperature modified, we now examine how the humidity increments contribute to the

Table 4. Specific Humidity Increments in the North

Pressure Level, hPa	Mean, %	SD, %	Number of Cases
400	−3	28	261
500	−12	30	251
600	−10	28	221
700	−10	23	150
850 hPa	−6	17	60

reduction of the innovation. We are interested in the transition below 10 km altitude from the 1DVAR T_SLP curve to the 1DVAR curve representing the residual (i.e., 1DVAR minus observation). In terms of bias, the largest differences between these two curves are located between the surface and 7–8 km altitude in Figure 10a. The 1DVAR T_SLP mean curve is positive in this region. Humidity has a local effect on refractivity as shown in equation (2). Contrary to temperature, the hydrostatic effect due to the replacement of dry air by lighter water vapor can be neglected in the present interpretation.

[88] The information content of the refractivity below 8–9 km altitude as constrained by the specified background error estimates is dominated by the water vapor information. The small temperature increments below 6 km do not reduce significantly the mean innovation in this region. Consequently, the 1DVAR should create negative humidity increments to compensate for the remaining positive difference in the 1DVAR T_SLP mean curve.

[89] Table 4 shows these increments in percent of the average of background and 1DVAR specific humidity. They agree with the postulation of the previous paragraph, i.e., negative mean humidity increments.

[90] We also see from Table 4 that the standard deviations of the humidity increments represent a significant portion of the assumed background uncertainties shown in Table 2. These somewhat large humidity increments are necessary to transform the 1DVAR T_SLP standard deviation curve in Figure 10b into the 1DVAR curve below 10 km altitude.

[91] We now discuss further the 1DVAR humidity comparisons with RS shown in Figure 8. Considering that the RS and the GPS refractivity represent in essence different averages, it is somewhat more difficult to demonstrate an impact of the GPS refractivity on the comparison between a humidity retrieved from a line averaged measurement and a point measured humidity. For the temperature, we have seen that this was not a problem, provided we showed that the 1DVAR temperatures were generally closer to the RS than the background. One possible explanation is the spatial variability of temperature, which is known to be in general less fine than that of humidity. Also, the intrinsically stronger variability of humidity would require a somewhat larger number of comparisons than temperature in order for the comparison to be as much representative as the comparisons involving temperature, whereas here we are in fact confronted with the opposite situation, i.e., a smaller number of available comparisons for the humidity than for the temperature, because of the highly variable quality of the RS humidities. More GPS data are required in order to establish a firm conclusion on the impact of GPS refractivity on the analysis of humidity. However, we have demonstrated that substantial increments have been made in the moisture fields after analysis of refractivity, and a small reduction in the 1DVAR minus RS standard deviation (as compared to background minus RS) has been showed at 700–400 hPa, although some degradation was observed below the 700-hPa level.

[92] To summarize how the increments are created in the present 1DVAR, we can state that (1) the humidity increments are dominant below 8–9 km (2) the SLP affects all altitudes significantly (3) temperature at and below the tropopause significantly affects the stratospheric residual. In this simplistic scheme, (1) is a local effect, whereas (2) and (3) correspond to a hydrostatic effect.

7. Conclusions and Future Directions

[93] In this paper, we discussed our implementation and assessment of a 1DVAR analysis of refractivity. Conceptually, the approach adjusts a background such that the refractivity of the solution matches the GPS observed refractivity, consistently with the background and the observational uncertainties.

[94] We compared GPS/MET refractivity data acquired in June–July 1995 with three backgrounds: 1995 GEOS Assimilation, and two versions of the next-generation FVDAS assimilation system. The first version of the FVDAS used the TOVS temperature retrievals produced by NESDIS, the second (FVDAS DAOTOVS) used interactively derived temperature and humidity retrievals from the TOVS radiances within the FVDAS. We examined and characterized the refractivity differences between these backgrounds and the GPS observations in terms of their mean and standard deviation. The standard deviations above the 300-hPa level are largest in the Southern Hemisphere reflecting the lack of radiosondes there and the heavy reliance on the forecast model in defining the vertical structure of the atmosphere. At lower altitudes, the standard deviations are much larger in the tropics and Northern hemisphere reflecting the much larger moisture concentrations in the warmer regions of the atmosphere. The utility of the GPS refractivity data as an independent benchmark data set for model validation studies is apparent in our results. The ''best'' expected of the three backgrounds (FVDAS DAOTOVS) exhibited the smallest mean discrepancies relative to GPS radio occultation observations. Furthermore, the agreement between the GPS and background results was noticeably worse in the radiosonde-sparse Southern Hemisphere. We used the FVDAS DAOTOVS forecasts as the background for the rest of our work.

[95] We applied the 1DVAR analysis method to GPS/MET summer 1995 refractivity data. We showed that, as expected, the 1DVAR refractivity profiles were much closer to the observed refractivity structure than the original background. In the Northern and Southern Hemispheres, we found that below 5 km altitude, discrepancies between the 1DVAR and GPS refractivity profiles were generally 0.4–0.6%. This suggests that the magnitude of the observational refractivity errors below 5 km altitude were smaller than the assumed observational errors developed by *Kursinski et al.* [1995, 1997] and used in our study.

[96] We discussed how the 1DVAR process uses discrepancies in the background minus observed refractivity

to adjust the background temperature, water vapor and sea-level pressure. The dependence of refractivity on these variables is both local and nonlocal depending on the variable. The dependence on water vapor content is essentially local. Therefore the 1DVAR makes local adjustments to moisture to reduce background versus observation refractivity discrepancies in the warmer, moist lower troposphere. The dependence of refractivity on sea-level pressure is quite nonlocal. Sea-level pressure adjustments are made when the vertical average of the discrepancies for a refractivity profile is significant. The 1DVAR reduces this average discrepancy by adjusting the entire atmospheric mass in the column by increasing or decreasing the sea-level pressure. The dependence of refractivity on temperature is both local and nonlocal. First, density and therefore refractivity depend inversely on local temperature, i.e., an increase in temperature will cause a local decrease in density and refractivity. Second, temperature has a nonlocal hydrostatic effect such that an increase in the analyzed temperature expands the atmosphere and increases the density and refractivity at higher altitudes. Therefore the 1DVAR will make local adjustments to temperature as well as temperature adjustments at lower altitudes to reduce density versus height discrepancies at higher altitudes.

[97] One of the potential strengths of GPS occultation observations is the ability to recover the geopotential height of pressure surfaces independent from radiosondes because unlike most passive observations, the independent coordinate is altitude (rather than pressure). With this expectation, the initial 1DVAR sea-level pressure adjustments found here were disappointing, although somewhat enlightening. The GPS/MET refractivity data caused the 1DVAR sea-level pressures to systematically decrease to values which are very unlikely to be correct based on comparisons with nearby radiosondes. The shift magnitudes were largest in the tropics (-2.6 hPa) and smallest in the Southern Hemisphere. The cause of these sea-level pressure biases turned out to be a subtle but significant bias between the observed vertical mean refractivity and that of the background. This bias is not unique to the background used here but has also been observed for ECMWF, UKMO, and NCEP refractivities as noted by *Kursinski et al.* [1996, 2000a], *Leroy* [1997], *Rocken et al.* [1997], and *Kursinski and Hajj* [2001].

[98] The 1DVAR temperature increments were significant. The standard deviation of the temperature adjustments in the Northern Hemisphere range from 0.4 K at 700 hPa and 0.8 K above 70 hPa to peak adjustments of $\sim$1.5 K at 200 hPa, approximately consistent with the vertical shape and magnitude of the background temperature error covariance. The standard deviations of Southern Hemisphere temperature adjustments were 1.5 to 2 times larger, reflecting how the background quality degrades in the absence of radiosondes. The standard deviations of tropical temperature adjustments were generally slightly larger than 1 K with a peak near 70 hPa consistent with the background error covariance.

[99] The 1DVAR produced a systematic, global adjustment in the vertical temperature structure with temperatures above the 300- to 400-hPa level being consistently shifted colder (~ -0.5 K) while those at lower altitudes were shifted warmer ($\sim$0.3 K). These systematic shifts were made to reduce the refractivity bias between the background and the GPS/MET observations.

[100] Comparisons with nearby radiosondes showed the 1DVAR temperatures presented an improvement over the background temperatures. The standard deviations were reduced throughout the 925- to 20-hPa interval by $\sim$0.2 K. The temperature bias relative to the radiosondes was also reduced with the exception of the 450- to 250-hPa interval and at 850 hPa.

[101] A limited number of radiosonde comparisons ($\sim$70) were made for the humidity, mostly in the Northern Hemisphere. These comparisons showed that the 1DVAR humidity presented a small dry bias, but larger than the background humidity bias when compared to RS. The 1DVAR solutions were systematically drier than the background (amounting to $\sim$10% in the North) because GPS refractivities are systematically lower than the background in the lower troposphere.

[102] Significant moisture increments were made by the 1DVAR in the warmer regions of the troposphere, with standard deviations ranging from 17% to 30% in the 850- to 400-hPa interval in the Northern Hemisphere. We showed that these increments contributed significantly to the reduction of the background minus GPS observations refractivity differences in the 1DVAR solutions below $\sim$10 km altitude. Based on the theoretical investigations of *Healy and Eyre* [2000] the 1DVAR humidity should have been improved when compared to the background humidity. Yet, the comparisons with RS showed that the 1DVAR minus RS humidity difference standard deviations were similar to the background minus RS humidity difference standard deviations, with small improvements observed between 550 and 400 hPa, and some degradation observed between the 850- and 700-hPa levels. This discrepancy suggests that some of our assumptions are not valid, for example, incorrect background and/or observation error covariance models and assumption of no bias in the 1DVAR theory.

[103] Even though there are assumptions made when deriving refractivity from bending angles (i.e., local spherical symmetry), we showed that in most cases GPS observations combined with a background in an accurate and computationally efficient 1DVAR framework yields significant improvement in terms of temperature. Mixed but encouraging results were obtained in terms of humidity. It is also worth noting that GPS will likely have larger impacts in remote regions devoid of radiosondes. We can see definite signs of this in the larger temperature increments in the Southern Hemisphere. Unfortunately, the lack of radiosondes in this region also means we cannot evaluate the impact via a radiosonde comparison.

[104] Whatever its source, the refractivity bias is a problem that must be confronted and solved for GPS occultation data to achieve its full impact in data assimilation and weather prediction. Finding the source of the bias also represents a critical step in the evaluation of the accuracy of the models, the GPS observations, and our present understanding of the vertical structure of the atmosphere.

[105] We have used in this study GPS/MET summer 1995 AS-off data, for which relatively few profiles probed to the

surface. We were limited in our RS comparison by very few radiosondes available in the Southern Hemisphere where the GPS occultations probing deepest occurred. We look forward to performing further investigations with new GPS data probing deeper in the troposphere and to carry out data assimilation experiments when more data are available. Quality control will have to be developed before radio occultation data can be routinely assimilated by data assimilation systems. As an extension to this study, the 1DVAR technique presented here can be improved to account for horizontal drifts and line-of-sight averaging in the observation operator. Aspects of the viewing geometry for these calculations were not provided in the GPS data set used here and should be made available by the data producers.

[106] **Acknowledgments.** We are grateful to the anonymous reviewers of this manuscript for their useful comments. We would also like to thank Data Assimilation Office members A. da Silva, D. Dee, S. Cohn for fruitful discussions, and Y. Kondratyeva for assistance with data sets used in the assimilation experiments.

References

Ahmad, B., and G. L. Tyler, Systematic errors in atmospheric profiles obtained from Abelian inversion of radio occultation data: Effects of large-scale horizontal gradients, *J. Geophys. Res.*, *104*, 3971–3992, 1999.

Bloom, S. C., L. L. Takacs, A. M. da Silva, and D. Ledvina, Data assimilation using incremental analysis updates, *Mon. Weather Rev.*, *124*, 1256–1271, 1996.

Cohn, S. E., A. da Silva, J. Guo, M. Sienkiewicz, and D. Lamich, Assessing the effects of data selection with the DAO physical-space statistical analysis system, *Mon. Weather Rev.*, *126*, 2913–2926, 1998.

Data Assimilation Office (DAO), Algorithm theoretical basis document (ATBD) version 2, Draft, NASA Goddard Space Flight Cent., Greenbelt, Md., 2000.

Dee, D. P., and A. M. da Silva, Data assimilation in the presence of forecast bias, *Q. J. R. Meteorol. Soc.*, *124*, 269–295, 1998.

Dee, D. P., and R. Todling, Data assimilation in the presence of forecast bias: The GEOS moisture analysis, *Mon. Weather Rev.*, *128*, 3268–3282, 2000.

Eyre, J. R., Assimilation of radio occultation measurements into a numerical weather prediction system, *Tech. Memo. 199*, ECMWF, Reading, England, 1994.

Eyre, J. R., G. A. Kelly, A. P. McNally, E. Andersson, and A. Persson, Assimilation of TOVS radiance information through one-dimensional variational analysis, *Q. J. R. Meteorol. Soc.*, *119*, 1427–1463, 1993.

Fjeldbo, G., A. J. Kliore, and V. R. Eshleman, The neutral atmosphere of Venus as studied with the Mariner V radio occultation experiments, *Astron. J.*, *76*, 123–140, 1971.

Gorbunov, M. E., and S. V. Sokolovskiy, Remote sensing of refractivity from space for global observations of atmospheric parameters, *Rep. 119*, Max Planck-Inst. für Meteorol., Hamburg, Germany, 1993.

Hajj, G. A., E. R. Kursinski, L. J. Romans, W. I. Bertiger, and S. S. Leroy, A technical description of atmospheric sounding by GPS occultation, *J. Atmos. Sol. Terr. Phys.*, *64*, 451–469, 2002.

Healy, S. B., A statistical comparison of GPS/MET radio occultation data with numerical weather prediction analyses, *Tech. Rep. 247*, 43 pp., UKMO Forecasting Res., Bracknell, UK, 1998.

Healy, S. B., and J. R. Eyre, Retrieving temperature, water vapour and surface pressure information from refractive index profiles derived by radio occultation: A simulation study, *Q. J. R. Meteorol. Soc.*, *126*, 1661–1683, 2000.

Hocke, K., Inversion of GPS meteorology data, *Ann. Geophys.*, *15*, 443–450, 1997.

Jazwinski, A. H., *Stochastic Processes and Filtering Theory*, 376 pp., Academic, San Diego, Calif., 1970.

Jenkins, J. M., P. G. Steffes, D. P. Hinson, J. D. Twicken, and G. L. Tyler, Radio occultation studies of the Venus atmosphere with the Magellan spacecraft, 2, Results from the October-1991 experiments, *Icarus*, *110*, 79–94, 1994.

Joiner, J., and L. Rokke, Variational cloud-clearing with TOVS data, *Q. J. R. Meteorol. Soc.*, *126*, 725–748, 2000.

Kuo, Y. H., S. V. Sokolovskiy, R. A. Anthes, and F. Vandenberghe, Assimilation of GPS radio occultation data for numerical weather prediction, *Terr. Atmos. Ocean. Sci.*, *11*, 157–186, 2000.

Kursinski, E. R., and G. A. Hajj, A comparison of water vapor derived from GPS occultations and global weather analyses, *J. Geophys. Res.*, *106*, 1113–1138, 2001.

Kursinski, E. R., G. A. Hajj, K. R. Hardy, L. J. Romans, and J. T. Schofield, Observing tropospheric water vapor by radio occultation using the global positioning system, *Geophys. Res. Lett.*, *22*, 2365–2368, 1995.

Kursinski, E. R., et al., Initial results of radio occultation observations of Earth's atmosphere using the global positioning system, *Science*, *271*, 1107–1110, 1996.

Kursinski, E. R., G. A. Hajj, J. T. Schofield, R. P. Linfield, and K. R. Hardy, Observing Earth's atmosphere with radio occultation measurements using the global positioning system, *J. Geophys. Res.*, *102*, 23,429–23,465, 1997.

Kursinski, E. R., S. B. Healy, and L. J. Romans, Initial results of combining GPS occultations with ECMWF global analyses within a 1DVar framework, *Earth Planets Space*, *52*, 885–892, 2000a.

Kursinski, E. R., G. A. Hajj, S. S. Leroy, and B. Herman, The GPS radio occultation technique, *Terr. Atmos. Ocean. Sci.*, *11*, 53–114, 2000b.

Leroy, S. S., Measurement of geopotential heights by GPS radio occultation, *J. Geophys. Res.*, *102*, 6971–6986, 1997.

Lin, S. J., A finite-volume integration method for computing pressure gradient force in general vertical coordinates, *Q. J. R. Meteorol. Soc.*, *123*, 1749–1762, 1997.

Lindal, G. F., The atmosphere of Neptune: An analysis of radio occultation data acquired with Voyager 2, *Astron. J.*, *103*, 967–982, 1992.

Lindal, G. F., H. B. Hotz, D. N. Sweetnam, Z. Shippony, J. P. Brenkle, G. V. Hartsell, and R. T. Spear, Viking radio occultation measurements of the atmosphere and topography of Mars — Data acquired during 1 Martian year of tracking, *J. Geophys. Res.*, *84*, 8443–8456, 1979.

Lindal, G. F., et al., The atmosphere of Jupiter — An analysis of the Voyager radio occultation measurements, *J. Geophys. Res.*, *86*, 8721–8727, 1981.

Lindzen, R. S., and M. Fox-Rabinovitz, Consistent vertical and horizontal resolution, *Mon. Weather Rev.*, *117*, 2575–2583, 1989.

Matsumura, T., J. C. Derber, J. G. Yoe, F. Vandenberghe, and X. Zou, The inclusion of GPS limb sounding into NCEP's global data assimilation system, *Off. Note 426*, NOAA/NWS/NCEP, Camp Springs, Md., 1999.

National Oceanic and Atmospheric Administration (NOAA), U.S. Standard Atmosphere 1976, 227 pp., U.S. Govt. Print. Off., Washington, D. C., 1976.

Palmer, P. I., Analysis of atmospheric temperature and humidity from radio occultation measurements, D. Phil. thesis, Oxford Univ., Oxford, England, 1998.

Palmer, P. I., and J. J. Barnett, Application of an optimal estimation inverse method to GPS/MET bending angle observations, *J. Geophys. Res.*, *106*, 17,147–17,160, 2001.

Palmer, P. I., J. J. Barnett, J. R. Eyre, and S. B. Healy, A non-linear optimal estimation inverse method for radio occultation measurements of temperature, humidity and surface pressure, *J. Geophys. Res.*, *105*, 17,513–17,526, 2000.

Pfaendtner, J., S. Bloom, D. Lamich, M. Seablom, M. Sienkiewicz, J. Stobie, and A. da Silva, Documentation of the Goddard Earth Observing System (GEOS) Data Assimilation System — version 1, *Tech. Memo. 104606-4*, NASA, Greenbelt, Md., 1995.

Poli, P., J. Joiner, and E. R. Kursinski, A one-dimensional variational analysis of GPS radio occultation refractivity, *Off. Note 2001-11*, Data Assimilation Off., NASA Goddard Space Flight Cent., Greenbelt, Md., 2001.

Reale, A. L., R. V. Wagener, and T. J. Gardner, TOVS operational sounding upgrades: 1990–1992, *Tech. Rep. 76*, NOAA/NESDIS, Washington, D. C., 1994.

Rocken, C., et al., Analysis and validation of GPS/MET data in the neutral atmosphere, *J. Geophys. Res.*, *102*, 29,849–29,866, 1997.

Rodgers, C. D., Retrieval of atmospheric temperature and composition from remote measurement of thermal radiation, *Rev. Geophys. Space Phys.*, *14*, 609–624, 1976.

Schubert, S., C. K. Park, C. Y. Wu, W. Higgins, Y. Kondratyeva, A. Molod, L. L. Takacs, M. Seablom, and R. Rood, A multi-year assimilation with the GEOS-1 system: Overview and results, *Tech. Memo. 104606-6*, NASA, Greenbelt, Md., 1995.

Smith, E. K., and S. Weintraub, The constants in the equation for atmospheric index at radio frequencies, *Proc. IRE*, *41*, 1035–1037, 1953.

Soden, B. J., and J. R. Lanzante, An assessment of satellite and radiosonde climatologies of upper tropospheric water vapor, *J. Clim.*, *9*, 1235–1250, 1996.

Steiner, A. K., G. Kirchengast, and H. P. Ladreiter, Inversion, error analysis and validation of GPS/MET occultation data, *Ann. Geophys.*, *17*, 122–138, 1999.

Takacs, L. L., A. Molod, and T. Wang, Documentation of the Goddard Earth Observing System (GEOS) General Circulation Model — version 1, *Tech. Memo. 104606-1*, NASA, Greenbelt, Md., 1994.

Tyler, G. L., V. R. Eshleman, J. D. Anderson, G. S. Levy, G. F. Lindal, G. E. Wood, and T. A. Croft, Radio science with Voyager-2 at Saturn — Atmosphere and ionosphere and the masses of Mimas, Tethys, and Iapetus, *Science*, *215*, 553–558, 1982.

Vorob'ev, V. V., and T. G. Krasil'nikova, Estimation of the accuracy of the atmospheric refractive index recovery from Doppler shift measurements at frequencies used in the NAVSTAR system, *Phys. Atmos. Ocean*, *29*, 602–609, 1994.

Ware, R. H., et al., GPS sounding of the atmosphere from low earth orbit: Preliminary results, *Bull. Am. Meteorol. Soc.*, *77*, 19–40, 1996.

Yunck, T. P., G. F. Lindal, and C. H. Liu, The role of GPS in precise Earth observation, paper presented at the Symposium on Position, Location and Navigation, Orlando, Florida, Nov. 29 to Dec. 2, 1988.

Zou, X., Y. H. Kuo, and Y. R. Guo, Assimilation of atmospheric radio refractivity using a non-hydrostatic adjoint model, *Mon. Weather Rev.*, *123*, 2229–2249, 1995.

Zou, X., B. Wang, H. Liu, R. A. Anthes, T. Matsumura, and Y. J. Zhu, Use of GPS/MET refraction angles in three-dimensional variational analysis, *Q. J. R. Meteorol. Soc.*, *126*, 3013–3040, 2000.

J. Joiner and P. Poli, Data Assimilation Office, Code 910.3, NASA Goddard Space Flight Center, Greenbelt, MD 20771, USA. (jjoiner@dao.gsfc.nasa.gov; ppoli@dao.gsfc.nasa.gov)

E. R. Kursinski, Department of Atmospheric Sciences, University of Arizona, Tucson, AZ 85721-0081, USA. (kursinsk@atmo.arizona.edu)